

Cite this: *J. Mater. Chem. A*, 2019, 7, 10431

Conductive metal–organic framework nanowire arrays for electrocatalytic oxygen evolution†

Wen-Hua Li,^{ab} Jiangquan Lv,^{ad} Qiaohong Li,^{id}^a Jiafang Xie,^a Naoki Ogiwara,^c Yiyin Huang,^a Huijie Jiang,^{ab} Hiroshi Kitagawa,^{id}^c Gang Xu^{id}^{*a} and Yaobing Wang^{id}^{*a}

The design and construction of efficient electrode materials are significant for electrochemical energy conversion and storage technologies. The oxygen evolution reaction (OER) is a key process in water splitting devices and metal–air batteries. Herein, we report conductive metal–organic framework (C-MOF) nanowire arrays on carbon cloth as a promising electrocatalyst for OER. The pyrolysis-free C-MOF electrocatalyst can maintain intrinsic molecular active sites in the MOFs. The as-prepared electrode possesses overpotentials of ~213 and 300 mV at 10 and 150 mA cm⁻² and long-term stability in 1 M KOH, respectively. Control experiments and Fourier-transform extended X-ray absorption fine structure (EXAFS) and Mössbauer spectra indicate that the Fe doped in the Ni-based MOFs may serve as highly effective OER active sites. Density functional theory (DFT) calculations reveal an unusual self-adaptable property of the Fe active sites, which enables the OER intermediates to generate additional hydrogen bonds with the neighboring layer, thus lowering the free energy in the OER process. Our findings may provide an alternative method for developing MOF electrocatalysts in frontier potential applications.

Received 26th February 2019

Accepted 26th March 2019

DOI: 10.1039/c9ta02169h

rsc.li/materials-a

Introduction

Electrochemical energy conversion and storage technologies are essential for sustainable development of human society.¹ The oxygen evolution reaction (OER) is a core process for renewable energy systems, such as water splitting and metal–air batteries.² However, the multistep proton-coupled electron transfer and multi-phase reaction in the OER process ($4\text{OH}^-(\text{aq}) \rightarrow 2\text{H}_2\text{O}(\text{l}) + \text{O}_2(\text{g}) + 4\text{e}^-$) hinder the development of high-performance electrocatalysts.³ Usually, efficient electrocatalysts require high conductivity/mass transfer and abundant accessible active sites as well as faster interface reactions. More importantly, decreasing the free energy of the OER intermediates at the interface would remarkably enhance the inherent electrochemical performance of a catalyst.⁴ For developing practical electrocatalysts and comprehending the origin of their activity,

both heterogeneous and homogeneous electrocatalysts have been developed with advanced results.⁵ Heterogeneous electrocatalysts take advantage of facile recovery but suffer from limited and indistinct active sites, especially in reaction environments;⁶ homogeneous electrocatalysts can utilize all active sites with identified structures but are limited by their difficult recovery.⁷

MOF materials as catalysts can combine the advantages of both homo- and heterogeneous catalysts. Unfortunately, most MOFs are insulating and are usually pyrolyzed to carbon or metal oxides to improve their electrical conductivity for electrocatalytic applications.⁸ However, this thermal treatment sacrifices the porous structures and intrinsic active metal sites of MOFs. Recently, MOFs with high electronic conductivity have emerged as new functional materials. In contrast with pyrolyzed MOF electrocatalysts, conductive metal–organic frameworks (C-MOFs) can be conveniently and directly utilized as electrocatalysts.⁹ Without the collapsed structures resulting from pyrolysis, C-MOFs provide the possibility to gain deep insight into the relationship between the structure and catalytic performance of MOFs. At present, MOFs prepared with triphenylene-derived ligands are the most studied C-MOFs. Triphenylene ligands have been used to feasibly devise planar pi-conjugated two-dimensional (2D) C-MOFs via the combination of “through-space” and “through-bond” strategies. The conductivity of the prepared 2D C-MOFs can be flexibly modulated from $\sim 10^{-6}$ to 4×10^1 S cm⁻¹ by modifying the triphenylene ligands and using disparate metal ions for different

^aState Key Laboratory of Structural Chemistry, Key Laboratory of Design and Assembly of Functional Nanostructures, Fujian Provincial Key Laboratory of Nanomaterials, Fujian Institute of Research on the Structure of Matter, Chinese Academy of Science, Yangqiao West Road 155#, Fuzhou, P. R. China. E-mail: gxu@fjirsm.ac.cn; wangyb@fjirsm.ac.cn

^bUniversity of Chinese Academy of Sciences, Beijing 100049, China

^cDivision of Chemistry, Graduate School of Science, Kyoto University, Kyoto, Japan

^dCollege of Electronics and Information Science, Organic Optoelectronics Engineering Research Center of Fujian's Universities, Fujian Jiangxia University, Fuzhou, Fujian 350108, P. R. China

† Electronic supplementary information (ESI) available. See DOI: 10.1039/c9ta02169h

application purposes.¹⁰ Very recently, this class of 2D C-MOFs has attracted considerable attention in the electrocatalytic field, such as hydrogen evolution reaction (HER) activity and the oxygen reduction reaction (ORR).¹¹ Hexahydroxytriphenylene ligand-based 2D C-MOFs possess M–O₄ (M, transition metals) as their secondary building units and provide discrete metal-replaceable layers as promising reactive sites for OER, in accordance with results from previous researchers.¹² Moreover, these 2D C-MOFs can remain stable in high pH solution, which was observed in previous research and is quite important for OER. Due to their structures and stability, these C-MOFs are very desirable but have yet to be studied as OER electrocatalysts.

Herein, we report a facile strategy to fabricate triphenylene-based 2D C-MOF Ni–HHTP nanowire arrays on carbon cloth as a high-performance OER electrocatalyst (HHTP, 2,3,6,7,10,11-hexahydroxytriphenylene). Ni–HHTP was directly *in situ* grown on the carbon cloth as nanowire arrays (NWA) for OER tests. Additionally, the OER performance of the Ni–HHTP NWA was significantly enhanced by substituting some Ni ions with Fe ions to create the catalyst Fe_xNi_y–HHTP NWA. The Fe₁Ni₄–HHTP NWA was studied and showed overpotentials of ~213 and 300 mV at 10 and 150 mA cm⁻², respectively, and excellent long-term stability in 1 M KOH. Control electrochemical experiments, Fourier transform extended X-ray absorption fine structure (EXAFS) spectra, Mössbauer spectra and density functional theory (DFT) calculations were used to reveal an unexpected “self-adaption active site” mechanism for this performance enhancement.

Results and discussion

Ni–HHTP NWA were directly grown on carbon cloth by immersing the carbon cloth into a reaction solution of Ni²⁺ and 2,3,6,7,10,11-hexahydroxytriphenylene (see Fig. S1a† and the Experimental section for details). Fe_xNi_y–HHTP NWA were synthesized by replacing some Ni ions with Fe ions in the above reaction. The feeding ratios of Fe/Ni were maintained at 0/1, 1/4, 1/2, 1/1, and 2/1. During the solvothermal process, the metal ions coordinate with the linkers through a co-crystallization process; then, Fe_xNi_y–HHTP MOF nanowires are formed (Fig. S1b†). The attempt to synthesize Fe–HHTP afforded an amorphous phase (Fig. S2†). The structure of Ni–HHTP comprises two distinct types of alternatively stacked layers in the trigonal space group *P* $\bar{3}c1$ (Fig. 1a, b and d). In one layer, the metal atom is coordinated to two HHTP linkers and two water molecules to form 2D extended honeycomb-like structures, and the other layer contains discrete units constructed from one HHTP ligand, three Ni ions and twelve water molecules. The layers stack in an overlapped fashion with the HHTP molecules in each layer rotated 30° with respect to each other. A hexagonal array of 1D channels with diameters of 1.8 nm is thus formed. Among the Fe_xNi_y–HHTP-based electrocatalysts, Fe₁Ni₄–HHTP showed the best OER performance and thus was used as an example for detailed characterization (Fig. S3†). In the powder X-ray diffraction patterns (PXRDs), Fe₁Ni₄–HHTP possesses identical peak positions to Ni–HHTP, demonstrating that they are isostructural and that Fe doping has a slight influence on

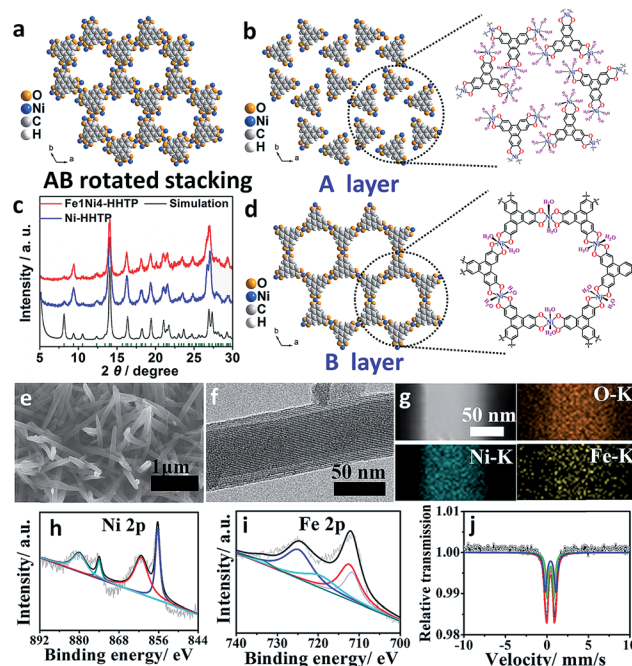


Fig. 1 (a) Space filling drawings of the packing structure of Ni–HHTP along the *c* direction (blue represents Ni, orange represents oxygen, grey represents carbon, and light grey represents hydrogen). (b, d) Space filling drawings of the discrete layer (A layer) and continuous layer (B layer), respectively. (c) PXRD patterns of Ni–HHTP and Fe₁Ni₄–HHTP and the simulated pattern. (e) SEM images of the Fe₁Ni₄–HHTP nanowire arrays grown on carbon cloth. (f) HRTEM images of the Fe₁Ni₄–HHTP nanowires. (g) HAADF-STEM image and corresponding O–K, Ni–K, and Fe–K STEM-EDX maps of the Fe₁Ni₄–HHTP nanowires. (h and i) XPS of the Fe₁Ni₄–HHTP nanowire arrays for (h) Ni 2p_{3/2} and Ni 2p_{1/2} and (i) Fe 2p_{3/2} and Fe 2p_{1/2}. (j) Mössbauer spectrum of Fe₁Ni₄–HHTP showing a Fe(III) signal with $\delta_1 = 0.43$ mm s⁻¹ and $\Delta EQ1 = 0.84$ mm s⁻¹, $\delta_2 = 0.43$ mm s⁻¹ and $\Delta EQ2 = 1.25$ mm s⁻¹.

their unit cell parameters (Fig. 1c, S4 and S5†). The crystal structures of Ni–HHTP and Fe₁Ni₄–HHTP were simulated based on their PXRDs by referring to a reported isostructural compound, Co-CAT.¹³ Conductivity measurements of Ni–HHTP in air with the powder pellet two-electrode method demonstrated its electron conducting nature, with a medium value of 3×10^{-3} S m⁻¹ (Fig. S6†). N₂ sorption measurements confirmed the porous structures of Ni–HHTP and Fe₁Ni₄–HHTP, which possess a pore size of ~1.8 nm (Fig. S7†). As shown in Fig. S8,† the blank carbon cloth (1 × 2 cm²) is gray and turns dark blue after being covered with Ni–HHTP or Fe₁Ni₄–HHTP NWA. The scanning electron microscopy (SEM) imaging (Fig. S9†) shows the smooth surface of the blank carbon cloth fibers with 10 μm diameters. After preparation, numerous oriented nanowires with high density uniformly covered the whole fibers (Fig. S10† and 1e).

The high-resolution transmission electron microscopy (HRTEM) images of Ni–HHTP and Fe₁Ni₄–HHTP (Fig. S11a, S12† and 1f) showed parallel-aligned channels in the nanowires; the spacing between two channels is close to 1.8 nm, suggesting that the preferred orientation is along (00*l*). The

high-angle annular dark-field (HAADF) image and the corresponding STEM-EDX map of a nanowire (Fig. S11b† and 1g) confirm the uniform distribution of Ni and O in Ni-HHTP as well as Ni, Fe and O in Fe1Ni4-HHTP. The inductively coupled plasma optical emission spectroscopy (ICP-OES) analysis reveals that 6.9% Ni was substituted by Fe in the Fe1Ni4-HHTP nanowires (Table S1†). The EDS results are shown in Fig. S13 and S14.† It can be observed that the elemental ratio of Fe/Ni measured by ICP-OES is not identical to the feeding ratio. This may result from the fact that the Fe^{3+} ions do not coordinate with HHTP ligands as readily as Ni^{2+} ions; therefore, some of the Fe^{3+} ions will not participate in the coordination process, leading to metal–ligand mismatches.¹⁵ The XPS spectra (Fig. 1h and i) and Mössbauer spectra (Fig. 1j) demonstrate the presence of Ni^{2+} and Fe^{3+} states in the Fe1Ni4-HHTP nanowires. The Ni 2p XPS spectra (Fig. 1h) show the characteristic spin-orbit peaks of Ni^{2+} . The binding peak at around 856.4 eV (Ni 2p_{3/2}) is attributed to the existence of Ni–oxygen bonds, and the peak at around 861.4 eV is the satellite of Ni 2p_{3/2}. The binding peaks at approximately 874.1 and 880.2 eV are assigned to Ni 2p_{1/2} and its satellite peak, respectively. The Fe 2p XPS spectra (Fig. 1i) show a peak at around 712.1 eV (2p_{3/2}), which is assigned to the Fe^{3+} oxidation state; the peak at 724.8 eV is attributed to 2p_{1/2}.

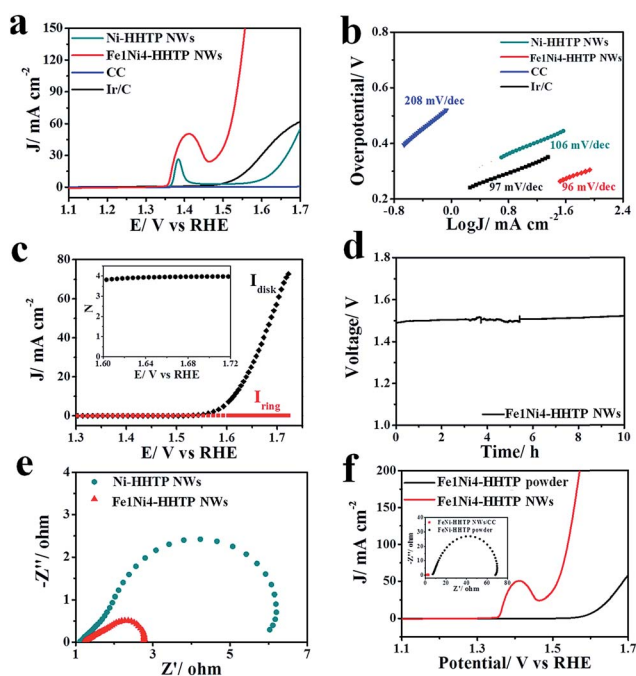


Fig. 2 (a) LSV curves and (b) Tafel plots of the Ni-HHTP NWs, Fe1Ni4-HHTP NWs, carbon cloth (CC), and Ir/C in 1 M KOH. (c) RRDE measurements for the OER of the Fe1Ni4-HHTP nanowire arrays in 1 M KOH at a 1600 rpm rotation rate under 1 atm N_2 without iR compensation; the inset figure shows the corresponding electron transfer number (N). (d) Chronopotentiometry curves of the Fe1Ni4-HHTP NWs *in situ* grown on carbon cloth in 1 M KOH at a current density of 30 mA cm^{-2} with iR correction. (e) Nyquist electrochemical impedance spectra of the Ni-HHTP NWs and Fe1Ni4-HHTP NWs grown on carbon cloth. (f) LSV curves of the Fe1Ni4-HHTP powder and nanowires grown on carbon cloth; the inset figure shows the corresponding Nyquist electrochemical impedance spectra.

The OER activity of the nanowire arrays was measured by linear scan voltammetry (LSV) in 1 M KOH (pH 14). As shown in Fig. 2a, the Ni-HHTP nanowire arrays acquired a current density of 10 mA cm^{-2} at 1.61 V (Fig. S15†), corresponding to $\sim 380 \text{ mV}$ overpotential. This further decreased to 213 mV after Fe doping, remarkably exceeding Ir/C (310 mV) as well as most recently reported MOF OER electrocatalysts (Table S2†). The additional peak at about 1.4 V is attributed to Ni^{2+} oxidation (confirmed by CV tests; see Fig. S16 and S17†), the positive shift of which is larger than that of Ni-HHTP; this implies that the incorporation of Fe suppresses the oxidation of Ni^{2+} .¹⁶ The Tafel plot of Ni-HHTP (Fig. 2b) exhibited a slope of 106 mV dec^{-1} . Upon doping with Fe, the slope decreased to 96 mV dec^{-1} , reflecting the enhanced electrochemical kinetics and the transfer of the rate-determining step from M-OH formation to M-O formation.¹⁷ The rotating ring-disk electrode (RRDE) technique revealed a four-electron pathway for water oxidation with 98.1% faradaic efficiency (FE) for O_2 generation (Fig. 2c and S18†). The Fe1Ni4-HHTP nanowire arrays showed remarkable stability, with only a 30 mV increase of potential after 10 h galvanostatic polarization at 30 mA cm^{-2} in 1 M KOH (Fig. 2d and S19–S21†). The electrochemical impedance spectra (Fig. 2e) further displayed charge transfer resistance at the electrode/electrolyte interface of 1.29Ω for the Fe1Ni4-HHTP nanowire arrays, which is much lower than that of Ni-HHTP (4.79Ω); this indicates a better charge transfer process in the Fe1Ni4-HHTP nanowire arrays. Moreover, the Fe1Ni4-HHTP nanowire arrays showed much better OER activity than the powder sample (Fig. 2f), which can be partially attributed to the lower ohmic resistance and charge transfer resistance (inset in Fig. 2f). Inspired by the excellent OER performance of Fe1Ni4-HHTP, a two-electrode electrolyzer using the Fe1Ni4-HHTP nanowire arrays on carbon cloth as the anode and commercial Pt/C as the cathode was demonstrated to require low voltages of $\sim 1.48 \text{ V}$ at 10 mA cm^{-2} current density and 1.68 V at 100 mA cm^{-2} (Fig. S22†). The water electrolyzer powered by a single-cell AA battery (voltage $\sim 1.5 \text{ V}$) and a commercial solar cell was also demonstrated (ESI Movie 1 and Fig. S23†) to have long-term stability. To evaluate the influence of introducing Fe element, we firstly investigated the morphology and electrochemical surface area (ECSA) modulation after Fe doping. The similar nanowire array morphology and ECSA (Fig. S24†) of the Fe1Ni4-HHTP nanowire arrays to those of Ni-HHTP suggest that its superior OER activity is due to the enhancement of intrinsic active sites by Fe doping. Interestingly, we found that the Ni-HHTP electrode showed remarkably enhanced OER activity after being dipped in the Fe^{3+} solution for 1 min (η_{10} decreased by 110 mV) (Fig. S25†). This implies that the enhanced activity may originate from the Fe active sites which are located at the edges or the discrete layers of Ni-HHTP. To further identify the location of the Fe atoms in Ni-HHTP, X-ray absorption near-edge structure (XANES) and extended X-ray absorption fine structure (EXAFS) analysis were carried out.

Fig. 3a illustrates the XANES spectra of Fe1Ni4-HHTP and its reference samples at the Fe K-edge. It was observed that Fe1Ni4-HHTP and Fe_2O_3 have similar response signals around the near-edge, which is obviously different from the Fe foil and FeO

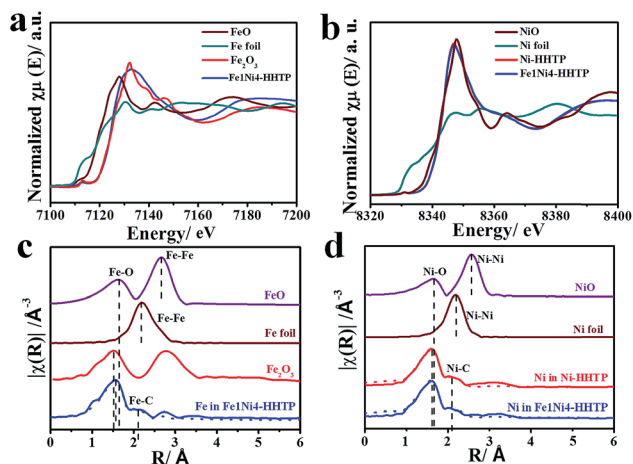


Fig. 3 (a) Fe K-edge XANES and (c) Fourier-transform EXAFS spectra of Fe1Ni4-HHTP and its references. (b) Ni K-edge XANES and (d) Fourier-transform EXAFS spectra of Ni-HHTP, Fe1Ni4-HHTP and their references. The blue and red dashed lines in (c) and (d) are the corresponding fitting curves (R range of 1 to 3 Å).

samples; this again confirms the Mössbauer analysis results of Fe^{3+} in Fe1Ni4-HHTP. The Ni K-edge XANES spectra (Fig. 3b) showed that Ni-HHTP and Fe1Ni4-HHTP had the same response signal around the near-edge (almost overlapping), indicating that introducing Fe did not alter the chemical structure of Ni^{2+} ion. Also, their signals resemble those of NiO, which is consistent with the XPS analysis results. The Fourier-transform EXAFS spectra in the R space and the best-fit analysis are summarized in Fig. 3c and d and S26 (details of the EXAFS fitting are shown in the ESI[†]). As shown in Fig. 3c and Table S3,[†] the dominant peak of Fe1Ni4-HHTP at 1.57 Å is very close to that of Fe_2O_3 (1.52 Å), indicating that Fe in Fe1Ni4-HHTP has the same $[\text{FeO}_6]$ octahedral coordination configuration as Fe_2O_3 . Furthermore, the peak at 2.12 Å was assigned to Fe-C in Fe1Ni4-HHTP, manifesting that the Fe atoms in Fe1Ni4-HHTP were coordinated with the ligand HHTP in the discrete layer. Further fitting of the peak at 1.61 Å of Ni-O in Fig. 3d also demonstrates the formation of the $[\text{NiO}_6]$ octahedral configuration. Ni in Ni-HHTP and Fe1Ni4-HHTP has nearly identical EXAFS spectra and fitting lines, suggesting that introducing Fe into Ni-HHTP does not affect the chemical environment of Ni in Ni-HHTP. However, the Ni-O distance ($R = 2.05$ Å) is larger than the Fe-O distance ($R = 2.01$ Å) in Fe1Ni4-HHTP, which may be caused by the larger radius and the weaker electrostatic attraction to negatively charged ligands of the Ni^{2+} ion compared with the Fe^{3+} ion in the environment of octahedral coordination.¹⁸ The above results together confirm that Fe atoms serving as active sites are coordinated with the ligand HHTP in the discrete layer of Fe1Ni4-HHTP. Furthermore, the extended π - π stacking structure of Fe1Ni4-HHTP benefits the electron transfer during the OER process.

To further understand the detailed effects of the Fe sites in Fe1Ni4-HHTP, DFT calculations were performed to investigate the electronic structures, OH^* , O^* , OOH^* adsorption free energies and variations of Gibbs free energy in the elementary

steps of OER on Fe1Ni4-HHTP and Ni-HHTP models. The possible active sites of Fe and Ni in diverse sites in the MOF were evaluated and calculated. We concluded that Fe replacing Ni in discrete units with potential open metal sites should be the active sites, in line with the experimental results. Fig. 4a displays the primitive steps of the OER process on Fe1Ni4-HHTP and reveals an unusual self-adaptable property of the Fe active sites, which enables the OER intermediates to generate additional hydrogen bonds with neighboring layers. Fig. 4b reveals that the formation of O^* requires the highest Gibbs free energy and becomes the rate-determining step (RDS) for OER. The Gibbs free energy for the RDS is 1.59 eV on Fe1Ni4-HHTP; this is lower than that on Ni-HHTP (1.76 eV), suggesting higher OER activity on the Fe sites than on the Ni sites. This corresponds with our experimental results, where Fe1Ni4-HHTP showed a much lower overpotential (210 mV at 10 mA cm^{-2}) than Ni-HHTP (380 mV at 10 mA cm^{-2}).¹⁹ To deeply understand this mechanism, further DFT and partial density of states (PDOS) calculations were investigated. Fig. 4c shows the partial densities of states (PDOS) of the intermediate O^* and the Fe/Ni active sites in Fe1Ni4-HHTP and Ni-HHTP, respectively. The profile of the d orbitals for Fe in Fe1Ni4-HHTP clearly shows a greater overlap with that of the O^* intermediate than that of Ni-HHTP.

It was demonstrated that the Fe- O^* interaction in Fe1Ni4-HHTP is stronger than the Ni- O^* interaction in Ni-HHTP. Fig. S27[†] shows that the Fe d orbitals are more involved in LUMO formation and that there is more involvement of the t_{2g} -like π^* Fe- O^* antibonding state than that of Ni- O^* , which benefits the stabilization of the key intermediate O^* on Fe1Ni4-

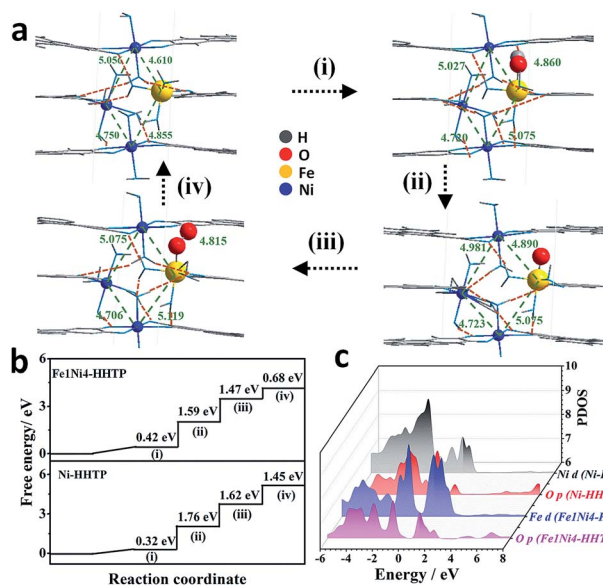


Fig. 4 (a) Primitive steps of the OER process on the Fe1Ni4-HHTP surface. Color scheme for chemical representation: blue for iron, green for nickel, red for oxygen, grey for carbon and white for hydrogen. (b) The free energy profiles for the OER pathway on the Fe1Ni4-HHTP and Ni-HHTP electrocatalysts, respectively. (c) Partial densities of states (PDOS) of O and Fe/Ni on the Fe1Ni4-HHTP and Ni-HHTP electrocatalysts, respectively.

HHTP. These findings illustrate that Fe sites have lower free energy in the OER process than Ni sites, leading to excellent OER activity; this is consistent with our experimental results and further confirms the predominant effect of the Fe active sites towards OER performance.

The simulated configurations of the initial state and three absorbed states (OH^* , O^* , and OOH^* intermediates) of $\text{Fe}_1\text{Ni}_4\text{-HHTP}$ and Ni-HHTP were compared. During the OER process on $\text{Fe}_1\text{Ni}_4\text{-HHTP}$ (Fig. S28[†]), the relative distance between Fe and two neighboring layer Ni increases first (OH^* absorbed), followed by a decrease (O^* absorbed), and then increases again (OOH^* absorbed), as listed in Table S4[†]; this demonstrates the self-adaptable position variation of Fe during OER. A similar phenomenon occurred in Ni-HHTP , but with more drastic variation (Fig. S29[†]). Upon further analysis, an additional hydrogen bond was found to form between the intermediates (OH^* and OOH^*) and the neighbor layer oxygen. Moreover, the stronger hydrogen bonds in the $\text{Fe}_1\text{Ni}_4\text{-HHTP}$ case (1.73 and 1.66 Å) than in Ni-HHTP (2.21 and 1.67 Å) can benefit the stabilization of OH^* and OOH^* (Fig. S30 and S31[†]) and also correspond to the shorter distance from the Fe active site to neighbor Ni in $\text{Fe}_1\text{Ni}_4\text{-HHTP}$ than in Ni-HHTP . These theoretical and experimental results clearly demonstrate that the self-adaptable position variance and additional hydrogen bonds both contribute to the stabilization of intermediates in the OER process, which is an efficacious way to develop high-performance catalysts.

Conclusions

In summary, an electronically conductive MOF, Ni-HHTP , was prepared with nanowire arrays and studied as an electrocatalyst for the first time. After replacing $\sim 6.9\%$ Ni^{2+} in the structure with Fe^{3+} , the electrocatalytic performance of the material significantly improved, showing overpotentials of ~ 213 and 300 mV at 10 and 150 mA cm^{-2} , respectively. More importantly, the impressive catalytic activity of $\text{Fe}_1\text{Ni}_4\text{-HHTP}$ is attributed to doping of Fe active sites in the discrete layer as well as the nanostructures, porosity and good conductivity of Ni-based MOFs, as demonstrated by electrochemical tests, EXAFS and Mössbauer characterizations. DFT calculations suggest that the Fe active sites exhibit an unexpected self-adaptable structure adjustment, enabling the OER intermediates to generate additional hydrogen bonds with adjacent layers and thus decreasing the free energy in the OER process. This will provide a new strategy for MOF electrocatalyst design and investigation *via* a combination of metal active sites and conductive MOF platforms.

Experimental

Synthesis of $\text{Fe}_x\text{Ni}_y\text{-HHTP}$ nanowire arrays ($x/y = 1/4, 1/2, 1/1, 2/1$)

In a typical synthesis of $\text{Fe}_1\text{Ni}_4\text{-HHTP}$, ferrous acetate (0.01 mmol, 1.74 mg), nickel acetate tetrahydrate (0.04 mmol, 9.95 mg), and HHTP (0.03 mmol, 9.8 mg) were dispersed in 1.5 mL of a solvent mixture of water/DMF ($v:v = 4:1$) under

sonication for 10 minutes in a 20 mL glass vial. A clean carbon cloth was immersed in the reaction solution, which was heated in an oven at 85 °C and then cooled to room temperature within 30 minutes. The length of the $\text{Fe}_1\text{Ni}_4\text{-HHTP}$ nanowire arrays was controlled by the reaction time. The $\text{Fe}_1\text{Ni}_4\text{-HHTP}$ nanowire array-coated carbon cloth was collected and washed thoroughly with deionized water 5 times and then treated by freeze-drying overnight. Then, the $\text{Fe}_1\text{Ni}_4\text{-HHTP}$ nanowire array-coated carbon cloth was immersed in DI water in a capped vial at 85 °C for 4 h. The same procedure was repeated with the final immersion step for 15 h. Then, the $\text{Fe}_1\text{Ni}_4\text{-HHTP}$ nanowire array-coated carbon cloth was dried under vacuum at 85 °C for 12 h. $\text{Fe}_1\text{Ni}_4\text{-HHTP}$ crystallite powder with an irregular morphology was collected at the bottom of the glass vial.

The $\text{Fe}_x\text{Ni}_y\text{-HHTP}$ nanowire arrays ($x/y = 1/2, 1/1, 2/1$) were synthesized by adopting similar procedures. For the preparation of $\text{Fe}_1\text{Ni}_2\text{-HHTP}$, $\text{Fe}_1\text{Ni}_1\text{-HHTP}$, and $\text{Fe}_2\text{Ni}_1\text{-HHTP}$, different initial molar ratios were used (the total mole number of metal ions was maintained at 0.05 mmol).

Synthesis of Ni-HHTP nanowire arrays

The Ni-HHTP nanowire arrays were synthesized as follows: nickel acetate tetrahydrate (0.05 mmol, 12.4 mg) and HHTP (0.03 mmol, 9.8 mg) were dispersed in 1.5 mL of a solvent mixture of water/DMF ($v:v = 4:1$) under sonication for 10 minutes in a 20 mL glass vial. The rest of the procedure was the same as that for the synthesis of $\text{Fe}_x\text{Ni}_y\text{-HHTP}$.

Synthesis of Fe-HHTP powder

Ferrous acetate (0.05 mmol, 8.7 mg) and HHTP (0.03 mmol, 9.8 mg) were dispersed in 1.5 mL of a solvent mixture of water/DMF ($v:v = 4:1$) under sonication for 10 minutes in a 20 mL glass vial. The rest of the procedure was the same as that for the synthesis of $\text{Fe}_x\text{Ni}_y\text{-HHTP}$.

Characterization

The morphologies of the as-prepared samples were observed by a scanning electron microscope (SEM, S4800/Cryo) equipped with an energy-dispersive spectroscopy analyzer. Transmission electron microscope (TEM) and HRTEM images were obtained by a JEM-2100F instrument at an acceleration voltage of 200 kV. The elements on the surfaces of our samples were identified by X-ray photoelectron spectroscopy (XPS, PerkinElmer PHI 5000C ESCA) with a monochromic $\text{Al/K}\alpha$ X-ray source. X-ray diffraction (XRD) was performed on a MiniFlex II diffractometer with $\text{Cu K}\alpha$ radiation ($\lambda = 1.54$ Å). The specific surface areas were measured through N_2 adsorption at 77 K using ASAP 2010 and calculated by the Brunauer-Emmett-Teller (BET) equation. The pore size distributions (PSD) were acquired based on the DFT (density functional theory) model.

X-ray absorption data collection, analysis and modeling

X-ray absorption spectra (XAS) were collected on the BL14B2 beam line at SPring-8 in transmission mode under ambient conditions with a Si (111) and Si (311) double crystal

monochromator for the Fe K-edge and Ni K-edge, respectively. To achieve the best signal-to-noise ratio, the powdered samples were uniformly mixed with BN powder and pressed into pellets (with diameters of 7 mm) to ascertain the edge jump of about 1.0. A detuning of about 20% by misaligning the silicon crystals was also performed to suppress the high harmonic content.

The as-obtained XAFS data were firstly processed in Athena (version 0.9.25) for background, pre-edge line and post-edge line calibration. The Fourier transform analysis was conducted with the Artemis (0.9.25) program. The data for Fe foil and Ni foil were first fitted with a fixed coordination number to determine the amplitude reduction factor ($S_0^2 = 0.77$ for Fe and $S_0^2 = 0.83$ for Ni) for the fitting of other samples. The k range was set between 3 and 15 \AA^{-1} , and the R range was 1 to 3 \AA . Independent CN and bond lengths were used for every shell, and the Debye–Waller factor and energy shift were shared for a dataset. A k weighting of 2 was used for all the fitting, and no parameters (CN, R , σ^2 , ΔE_0) were fixed.

For wavelet transform analysis, the $\chi(k)$ exported from Athena was imported into the Hama Fortran code. The parameters were as follows: R range, 1 to 3 \AA , k range, 2 to 15 \AA^{-1} and k weight, 2; also, a Morlet function with $\kappa = 18$, $\sigma = 1$ was used as the mother wavelet to provide the overall distribution.

The following equation was used to calculate and fit the RFD of Ni–HHTP and Fe1Ni4–HHTP:

$$\chi(k) = S_0^2 \sum \frac{N_j f_j(k) \exp[-2\kappa^2 \sigma_j^2]}{\kappa r_j^2} \sin[2\kappa r_j + \delta(k)]$$

where r is the distance from the target to the neighboring atom, N is the coordination number of the neighboring atom, and σ^2 is the Debye–Waller factor. The photoelectron wavenumber κ is given as $\sqrt{2m[E - E_0]/\hbar^2}$, $f(k)$ is the scattering amplitude, and $\delta(k)$ is the phase shift. S_0 is the amplitude reduction factor. The EXAFS spectra of Ni–HHTP and Fe1Ni4–HHTP were fitted in the r range from 1.00 to 3.00 \AA . The final values of these parameters are summarised in Table S3.†

Electrochemical measurements

Electrochemical measurements were performed in a three-electrode electrochemical setup using a computer-controlled electrochemistry workstation (CHI 660E, CH Instrument Inc.). A platinum wire electrode and an Ag/AgCl-saturated KCl electrode served as the counter and reference electrode, respectively. Linear sweep voltammetry (LSV) was performed with a potential range from 0 to 0.7 V vs. Ag/AgCl for OER activity measurements, which were conducted in 1 M KOH solution at a scan rate of 10 mV s⁻¹. The potentials reported in this study are all quoted against the reversible hydrogen electrode (RHE) using the equation E vs. RHE = E (Ag/AgCl) + 0.197 + 0.059 × pH. All polarization curves were corrected with 90% iR -compensation. The long-term stability of the electrocatalysts was measured by chronopotentiometry tests at 30 mA cm⁻². We also conducted rotating ring disc electrode (RRDE) experiments to determine the electron transfer numbers and Faraday efficiency. The electron transfer numbers were determined by

applying a constant potential of 1.4 V (vs. RHE) to a ring electrode:

$$n = \frac{4I_d}{I_r/N + I_d}$$

The faradaic efficiency of the OER system was determined by applying a constant potential of 0.4 V (vs. RHE) to the ring electrode:

$$\varepsilon = \frac{2I_r}{N \times I_d}$$

where I_d , I_r , N and n are the disk current, ring current, collection efficiency and the number of electrons transferred per O₂ molecule in ORR, respectively. Here, the value of N is taken to be 0.37.

Electrochemical capacitance was determined using cyclic voltammetry (CV), which was performed over a potential window of -0.16 to -0.06 V vs. Ag/AgCl (open-circuit potential: -0.11 V) and scan rates ranging from 5 to 800 mV s⁻¹. EIS was recorded under the following conditions: AC voltage amplitude 1.5 V vs. RHE, frequency range 106 to 0.1 Hz. The resistant values were the fits to the data using the simplified Randle's circuit. The conductivities of the MOF powder pellets were measured with a two-probe method using a Keithley 4200 instrument (Fig. S4†). The pellets of MOFs were pressed at a pressure of approximately 1 GPa. Electrical measurements were performed using a two-electrode setup in air at a constant temperature of 297 K and in the absence of light.

Water splitting devices and measurements

For the preparation of the water splitting electrodes, the Fe1Ni4–HHTP nanowire array on carbon cloth was directly used as the anode and the cathode was prepared by coating commercial Pt/C on 1 cm² carbon cloth with a loading of 1 mg cm⁻². The water electrolysis could be powered by a single-cell AA battery (voltage ~ 1.5 V). This was demonstrated by coupling a commercial planar polycrystalline Si solar cell with a two-electrode water electrolyzer setup for the direct utilization of solar energy in water splitting. The Si solar cell with geometric dimensions of 14.6 cm² presented a short circuit current density of 5 mA cm⁻² and an open circuit potential of 2.0 V.

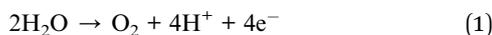
DFT calculations

The electronic structures of all the catalysts were computed using the Dmol3 package.^{20,21} All calculations were performed with the PBE exchange–correlation functional (the 1996 functional of Perdew, Burke and Ernzerhof) on periodically repeated slabs.²² The double-numeric quality basis set with polarization functions (DNP) was adopted.^{23,24} Numerical basis sets can minimise the basis-set superposition error.²⁵ A Fermi smearing of 0.005 hartree was utilized. The tolerances of the energy, gradient and displacement convergence were 1 × 10⁻⁵ hartree, 2 × 10⁻³ hartree per \AA , and 5 × 10⁻³ \AA , respectively. We used one ABA–Fe cluster and ABA–Ni cluster. One discrete layer (B)

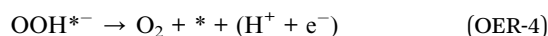
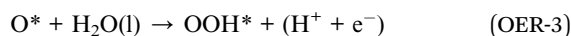
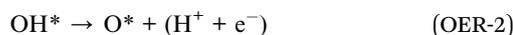
with numerous coordinatively unsaturated metal atoms was sandwiched by two extended layers to form the ABA cluster. All structures were fully relaxed to the ground state.

Microkinetic analysis

The microkinetic process of the water-splitting reaction was modeled with the approach used by Nørskov and coworkers,^{26–28} which has been recently applied to two-dimensional phosphorus porous polymorphs,²⁹ graphitic carbon nitride-supported single-atom catalysts³⁰ and carbon nitride monolayers.³¹ The two half-reaction equations, *i.e.* OER and HER, are listed below:



For OER, eqn (1) is decomposed into four one-electron steps, (OER-1) to (OER-4), where each step generates one H^+ and an electron, as listed below:



The Gibbs free energy change (ΔG_i) of each reaction step can be described as

$$\Delta G_i = \Delta E_i + \Delta \text{ZPE}_i + T\Delta S_i + \Delta G_u + \Delta G_{\text{pH}}$$

where ΔE_i represents the DFT-calculated reaction energy, ΔZPE_i refers to the zero point energy change, T is the temperature, ΔS_i is the entropy change, $\Delta G_u = -eU$ (where U is the potential of the photogenerated electrons/holes with respect to the normal hydrogen electrode (NHE)) and $\Delta G_{\text{pH}} = 2.303k_{\text{B}}T \times \text{pH}$ (where k_{B} is the Boltzmann constant). The entropies of the free molecules were taken from the NIST database (<http://cccbdb.nist.gov/>), and the energy contribution from the configuration entropy in the adsorbed state was not included. As a generally accepted OER activity descriptor, the overpotential (η) for a chemical reaction can be calculated as follows:

$$\eta = \max[\Delta G_1, \Delta G_2, \Delta G_3, \Delta G_4]/e - 1.23[\text{V}]$$

This is independent of pH and is therefore applicable to water-alkali conditions.

Conflicts of interest

There are no conflicts to declare.

Acknowledgements

This work was supported by the National Key R&D Program of China (2017YFA0206802 and 2016YFB0100100), the NSFC (21501173, 21822109, 21603229, 21771177, 21601190, 21872147 and 21805277, 21773245), the NSFC of Fujian Province (2014J05027 and 2016J01080 and 2018J05030), the Strategic Priority Research Program of the CAS (XDB20000000), the Key Research Program of Frontier Sciences, CAS (QYZDB-SSW-SLH019 and QYZDB-SSW-SLH023), the International Partnership Program of CAS (121835KYSB201800), and the Science and Technology Planning Project of Fujian Province (2014H2008). We are thankful to Dr Tetsuo of JASRI for technical support during the collection of XAS. The XAS measurements were performed with the approval of JASRI (Proposal No. 2018B1728).

References

- (a) T. R. Cook, D. K. Dogutan, S. Y. Reece, Y. Surendranath, T. S. Teets and D. G. Nocera, *Chem. Rev.*, 2010, **110**, 6474–6502; (b) S. Chu and A. Majumdar, *Nature*, 2012, **488**, 294–303.
- (a) M. Tahir, L. Pan, F. Idrees, X. W. Zhang, L. Wang, J. J. Zou and Z. L. Wang, *Nano Energy*, 2017, **37**, 136–157; (b) A. Grimaud, O. Diaz-Morales, B. H. Han, W. T. Hong, Y. L. Lee, L. Giordano, K. A. Stoerzinger, M. T. M. Koper and Y. Shao-Horn, *Nat. Chem.*, 2017, **9**, 457–465; (c) J. Fu, Z. P. Cano, M. G. Park, A. P. Yu, M. Fowler and Z. W. Chen, *Adv. Mater.*, 2017, **29**, 1604685; (d) B. You and Y. Sun, *Acc. Chem. Res.*, 2018, **51**(7), 1571–1580; (e) C. Zhu, Z. Yin, W. Lai, Y. Sun, L. Liu, X. Zhang, Y. Chen and S.-L. Chou, *Adv. Energy Mater.*, 2018, **8**, 1802327; (f) Y. Wu, X. Tao, Y. Qing, H. Xu, F. Yang, S. Luo, C. Tian, M. Liu and X. Lu, *Adv. Mater.*, 2019, 1900178.
- (a) Y. Zhang, H. Zhang, A. Liu, C. Chen, W. Song and J. Zhao, *J. Am. Chem. Soc.*, 2018, **140**(9), 3264–3269; (b) N. T. Suen, S. F. Hung, Q. Quan, N. Zhang, Y. J. Xu and H. M. Chen, *Chem. Soc. Rev.*, 2017, **46**, 337–365; (c) B. M. Hunter, H. B. Gray and A. M. Muller, *Chem. Rev.*, 2016, **116**, 14120–14136; (d) M. G. Walter, E. L. Warren, J. R. McKone, S. W. Boettcher, Q. Mi, E. A. Santori and N. S. Lewis, *Chem. Rev.*, 2010, **110**, 6446–6473.
- Z. W. Seh, J. Kibsgaard, C. F. Dickens, I. B. Chorkendorff, J. K. Nørskov and T. F. Jaramillo, *Science*, 2017, **355**, ead4998.
- (a) K. N. Ferreira, T. M. Iverson, K. Maghlaoui, J. Barber and S. Iwata, *Science*, 2004, **303**, 1831–1838; (b) C. C. L. McCrory, S. H. Jung, J. C. Peters and T. F. Jaramillo, *J. Am. Chem. Soc.*, 2013, **135**, 16977–16987; (c) T. J. Meyer, M. V. Sheridan and B. D. Sherman, *Chem. Soc. Rev.*, 2017, **46**, 6148–6169; (d) J. Li, R. Güttinger, R. Moré, F. Song, W. Wan and G. R. Patzke, *Chem. Soc. Rev.*, 2017, **46**, 6124–6147; (e) H. B. Aiyappa, J. Thote, D. B. Shinde, R. Banerjee and S. Kurungot, *Chem. Mater.*, 2016, **28**(12), 4375–4379; (f) H. Schäfer and M. Chatenet, *ACS Energy Lett.*, 2018, **3**(3), 574–591; (g) H. Schäfer, S. Sadaf, L. Walder, K. Kuepper, S. Dinklage, J. Wollschläger, L. Schneider, M. Steinhart,

- J. Hardege and D. Daum, *Energy Environ. Sci.*, 2015, **8**, 2685–2697; (h) X. Huang, S. Chang, W. S. V. Lee, J. Ding and J. M. Xue, *J. Mater. Chem. A*, 2017, **5**, 18176–18182; (i) H. Schäfer, K. Küpper, M. Schmidt, K. Müller-Buschbaum, J. Stangl, D. Daum, M. Steinhart, C. Schulz-Kölbel, W. Han, J. Wollschläger, U. Krupp, P. Hou and X. Liu, *Catal. Sci. Technol.*, 2018, **8**, 2104–2116; (j) S. Anantharaj, M. Venkatesh, A. S. Salunke, T. V. S. V. Simha, V. Prabu and S. Kundu, *ACS Sustainable Chem. Eng.*, 2017, **5**(11), 10072–10083.
- 6 J. S. Kim, B. Kim, H. Kim and K. Kang, *Adv. Energy Mater.*, 2018, **8**, 1702774.
- 7 J. Li, R. Guttinger, R. More, F. Song, W. Wan and G. R. Patzke, *Chem. Soc. Rev.*, 2017, **46**, 6124–6147.
- 8 (a) J. Zhu, M. Xiao, Y. Zhang, Z. Jin, Z. Peng, C. Liu, S. Chen, J. Ge and W. Xing, *ACS Catal.*, 2016, **6**(10), 6335–6342; (b) B. Y. Guan, X. Y. Yu Hao, B. Wu and X. W. Lou, *Adv. Mater.*, 2017, **29**, 1703614; (c) N. Cheng, L. Ren, X. Xu, Y. Du and S. X. Dou, *Adv. Energy Mater.*, 2018, 1801257–1801277; (d) T. Palaniselvam, B. P. Biswal, R. Banerjee and S. Kurungot, *Chem.–Eur. J.*, 2013, **19**(28), 9335–9342.
- 9 W. Wang, X. Xu, W. Zhou and Z. Shao, *Adv. Sci.*, 2017, **4**, 1600371.
- 10 R. Dong, Z. Zhang, D. C. Tranca, S. Zhou, M. Wang, P. Adler, Z. Liao, F. Liu, Y. Sun, W. Shi, Z. Zhang, E. Zschech, S. C. B. Mannsfeld, C. F. Felser and X. Feng, *Nat. Commun.*, 2018, **9**, 2637.
- 11 (a) E. M. Miner, T. Fukushima, D. Sheberla, L. Sun, Y. Surendranath and M. Dincă, *Nat. Commun.*, 2016, **7**, 10942; (b) A. J. Clough, J. W. Yoo, M. H. Mecklenburg and S. C. Marinescu, *J. Am. Chem. Soc.*, 2015, **137**(1), 118–121; (c) R. Dong, Z. Zheng, D. C. Tranca, J. Zhang, N. Chandrasekhar, S. Liu, X. Zhuang, G. Seifert and X. Feng, *Chem.–Eur. J.*, 2017, 2255.
- 12 (a) X.-H. Liu, W.-L. Hu, W.-J. Jiang, Y.-W. Yang, S. Niu, B. Sun, J. Wu and J.-S. Hu, *ACS Appl. Mater. Interfaces*, 2017, **9**, 28473–28477; (b) M. Zhang, B.-H. Zheng, J. Xu, N. Pan, J. Yu, M. Chen and H. Cao, *Chem. Commun.*, 2018, **54**, 13579.
- 13 M. Hmadeh, Z. Lu, Z. Liu, F. Gandara, H. Furukawa, S. Wan, V. Augustyn, R. Chang, L. Liao, F. Zhou, E. Perre, V. Ozolins, K. Suenaga, X. F. Duan, B. Dunn, Y. Yamamoto, O. Terasaki and O. M. Yaghi, *Chem. Mater.*, 2012, **24**, 3511–3513.
- 14 L. Sun, M. G. Campbell and M. Dinca, *Angew. Chem., Int. Ed.*, 2016, **55**, 2–16.
- 15 J. Li, W. Huang, M. Wang, S. Xi, J. Meng, K. Zhao, J. Jin, W. Xu, Z. Wang, X. Liu, Q. Chen, L. Xu, X. Liao, Y. Jiang, K. A. Owusu, B. Jiang, C. Chen, D. Fan, L. Zhou and L. Mai, *ACS Energy Lett.*, 2019, **4**, 285–292.
- 16 M. W. Louie and A. T. Bell, *J. Am. Chem. Soc.*, 2013, **135**, 12329–12337.
- 17 T. Shinagawa, A. T. Garcia-Esparza and K. Takanahe, *Sci. Rep.*, 2015, **5**, 13801.
- 18 D. Friebel, M. W. Louie, M. Bajdich, K. E. Sanwald, Y. Cai, A. M. Wise, M.-J. Cheng, D. Sokaras, T.-C. Weng, R. A.-M. Mori, R. C. Davis, J. R. Bargar, J. K. Nørskov, A. Nilsson and A. T. Bell, *J. Am. Chem. Soc.*, 2015, **137**, 1305–1313.
- 19 S. L. Zhao, Y. Wang, J. C. Dong, C. T. He, H. J. Yin, P. F. An, K. Zhao, X. F. Zhang, C. Gao, L. J. Zhang, J. W. Lv, J. X. Wang, J. Q. Zhang, A. M. Khattak, N. A. Khan, Z. X. Wei, J. Zhang, S. Q. Liu, H. J. Zhao and Z. Y. Tang, *Nat. Energy*, 2016, **1**, 1–10.
- 20 B. Delley, *J. Chem. Phys.*, 1990, **92**(1), 508–517.
- 21 B. Delley, *J. Chem. Phys.*, 2000, **113**(18), 7756–7764.
- 22 J. P. Perdew, K. Burke and M. Ernzerhof, *Phys. Rev. Lett.*, 1996, **77**(18), 3865–3868.
- 23 L. Versluis and T. Ziegler, *J. Chem. Phys.*, 1988, **88**(1), 322–328.
- 24 U. Von Barth and L. Hedin, *J. Phys. C: Solid State Phys.*, 1972, **5**(13), 1629.
- 25 N. Matsuzawa, J. Seto and D. A. Dixon, *J. Phys. Chem. A*, 1997, **101**(49), 9391–9398.
- 26 J. K. Nørskov, J. Rossmeisl, A. Logadottir, L. Lindqvist, J. R. Kitchin, T. Bligaard and H. Jónsson, *J. Phys. Chem. B*, 2004, **108**(46), 17886–17892.
- 27 J. Rossmeisl, Z.-W. Qu, H. Zhu, G.-J. Kroes and J. K. Nørskov, *J. Electroanal. Chem.*, 2007, **607**(1–2), 83–89.
- 28 Á. Valdés, Z.-W. Qu, G.-J. Kroes, J. Rossmeisl and J. K. Nørskov, *J. Phys. Chem. C*, 2008, **112**(26), 9872–9879.
- 29 Z. Zhuo, X. Wu and J. Yang, *J. Am. Chem. Soc.*, 2016, **138**(22), 7091–7098.
- 30 X. Li, P. Cui, W. Zhong, J. Li, X. Wang, Z. Wang and J. Jiang, *Chem. Commun.*, 2016, **52**(90), 13233–13236.
- 31 J. Wirth, R. Neumann, M. Antonietti and P. Saalfrank, *Phys. Chem. Chem. Phys.*, 2014, **16**(30), 15917–15926.